Mon. Not. R. Astron. Soc. **287,** 833–847 (1997)

Lensing by galaxy haloes in clusters of galaxies

Priyamvada Natarajan[1] and Jean-Paul Kneib[2]

[1]*Institute of Astronomy, Madingley Road, Cambridge CB3 0HA*

[2]*Observatoire Midi-Pyrenees, 14 Av. E. Belin, 31400 Toulouse, France*

Accepted 1997 January 9. Received 1996 December 2; in original form 1996 September 3

ABSTRACT

Weak shear maps of the outer regions of clusters have been successfully used to map the distribution of mass at large radii from the cluster centre. The typical smoothing lengths employed thus far preclude the systematic study of the effects of galactic-scale substructure on the measured weak lensing signal. In this paper, we present two methods to infer the possible existence and extent of dark haloes around bright cluster galaxies by quantifying the 'local' weak lensing induced by them. The proposed methods are: direct radial averaging of the shear field in the vicinity of bright cluster members, and a maximum likelihood method to extract fiducial parameters characterizing galaxy haloes. The correlations observed for early-type galaxies on the Fundamental Plane are used to derive the scaling laws with luminosity in the modelling of cluster galaxies. We demonstrate using simulations that these observed local weak shear effects on galactic scales within the cluster can be used to constrain statistically the mean mass-to-light ratio, and fiducial parameters like the halo size, velocity dispersion and hence mass of cluster galaxies. We compare the two methods and investigate their relative drawbacks and merits in the context of feasibility of application to *HST* cluster data, whereby we find that the prospects are promising for detection on stacking a minimum of 20 WFPC2 deep cluster fields.

Key words: galaxies: clusters: general – gravitational lensing – large-scale structure of Universe.

1 INTRODUCTION

Clusters of galaxies are the most recently assembled structures in the Universe, and the degree of observed substructure in a cluster is the result of the complex interplay between the underlying cosmological model [as has been demonstrated by many groups including Bird (1993), Evrard et al. (1993) and West & Bothun (1990)] and the physical processes by which clusters form and evolve. Many clusters have more than one dynamical component in the velocity structure in addition to spatial subclustering (Colless & Dunn 1996; Kriessler, Beers & Odewahn 1995; Bird 1993; West & Bothun 1990; Fitchett 1988). Substructure in the underlying cluster potential and specifically the subclumping of mass on smaller scales (galactic scales) within the cluster can be directly mapped via lensing effects.

The observed gravitational lensing of the faint background population by clusters is increasingly becoming a promising probe of the detailed mass distribution within a cluster as well as on larger scales (super-cluster scales). We expect on theoretical grounds, and do observe, local weak shear effects around individual bright galaxies in clusters over and above the global shearing produced by the 'smooth' cluster potential. While there is ample evidence from lensing for the clumping of dark matter on different scales within the cluster, the spatial extent of dark haloes of cluster galaxies is yet to be constrained. The issue is of crucial importance as it addresses the key question of whether the mass-to-light ratio of galaxies is a function of the environment, and if it is indeed significantly different in the high-density regions like cluster cores as opposed to the field. Moreover, it is the physical processes that operate within clusters, like ram-pressure stripping, merging and 'harassment', that imply re-distribution of mass on smaller scales, and their efficiency can be directly probed using accurate lensing mass profiles.

Constraining the fundamental parameters such as mass and halo size from lensing effects for field galaxies was attempted first by Tyson et al. (1984) using plate material, the quality of which precluded any signal detection. More recently, Brainerd, Blandford & Smail (1996) used deep ground-based imaging, and detected the galaxy–galaxy lensing signal and hence placed upper limits on the mean mass of an average field galaxy. Griffiths et al. (1996) used the Medium Deep Survey (MDS) and *HST* archival data in a similar manner to extract the polarization signal. Although the signal is unambiguously detected, it is weak, and no strong constraints can yet be put on the mean profile of field galaxies, but the prospects are promising for the near future.

On the other hand, no such analysis has been pursued in dense regions like clusters, and very little is known about the lensing effect of galaxy haloes superposed on the lensing effect of a cluster. Kneib et al. (1996) have demonstrated the importance of galactic-scale lenses in the mass modelling of the cluster A2218, where the effect of galactic-scale components (with a mean mass-to-light ratio ~ 9 in the R band) needs to be included in order to reproduce the observed multiple images. Mass modelling of several other clusters has also required the input of smaller-scale mass components to explain consistently the multiple images as well as the geometry of the arcs, for instance, in the case of CL0024 (Kassiola, Kovner & Fort 1993; Smail et al. 1995a), where the length of the three images of the cusp arc can only be explained if the two nearby bright galaxies contribute mass to the system. This strongly suggests that the dark matter associated with individual galaxies is of consequence in accurately mapping the mass distribution, and needs to be understood better, particularly if clusters are to be used as gravitational telescopes to study background galaxies.

The observed quantities in cluster lensing studies are the magnitudes and shapes of the background population in the field of the cluster. To reconstruct the cluster mass distribution, there are many techniques currently available which allow the inversion of the distortion map into a relative mass map or an absolute mass map if (i) multiple arcs are observed (Kneib et al. 1996) and or (ii) magnification effects are included (Broadhurst, Taylor & Peacock 1995). Recent theoretical work (Kaiser & Squires 1993; Kaiser 1995; Schneider 1995; Schneider & Seitz 1995; Squires & Kaiser 1995) has focused on developing various algorithms to recover the mass distribution on scales larger than 20–30 arcsec, which is roughly the smoothing scale employed (corresponding to $\sim$100 kpc at a redshift of $z \sim 0.2$). These methods involve locally averaging the shear field produced by the lensing mass, and cannot be used to probe galactic-scale perturbations to the shear field.

Our aim in this paper is to understand and determine the parameters that characterize galactic-scale perturbations within a cluster. In order to do so, we delineate two regimes: (i) the 'strong' regime where the local surface density is close to critical ($\kappa \sim 1$, where κ is the ratio of the local surface density to the critical surface density) and (ii) the 'weak' regime where the local surface density is small ($\kappa < 1$). The 'strong' regime corresponds to the cores of clusters, and in general involves only a small fraction (typically 5–20) of the cluster galaxies, whereas the 'weak' regime encompasses a larger fraction ($\sim$ 50–200). We are restricting our treatment to early-type (Es & S0s) bright cluster galaxies throughout.

We compare in this analysis the relative merits of our two proposed methods: a direct method to extract the strength of the averaged local shear field in the vicinity of bright cluster galaxies by subtracting the mean large-scale shear field, and a statistical maximum likelihood method. The former method affords us a physical understanding, helps to establish the importance and the role of the various relevant parameters and yields a mean mass-to-light ratio; the latter permits us to take the strong lensing regime and the ellipticity of the mass of galaxy haloes into account correctly. Both approaches are investigated in detail in this paper using numerical simulations.

The outline of the paper is as follows. In Section 2, we present the formalism that takes into account the effect of individual galactic-scale perturbations to the global cluster potential. In Section 3, the direct method to recover these small-scale distortions is outlined, and in Section 4 we present the results of the application of these techniques to a simulated cluster with substructure. In Section 5, we examine the constraints that can be obtained on the parameter space of models via the proposed maximum likelihood method. We also explore the feasibility criteria for application to cluster data given the typical uncertainties. The conclusions of this study and the prospects for application to real data and future work are discussed in Section 6. Throughout this paper, we have assumed $H_0 = 50\,\mathrm{km\,s^{-1}Mpc^{-1}}$, $\Omega = 1$ and $\Lambda = 0$.

2 GALAXY-SCALE LENSING DISTORTIONS IN CLUSTERS

2.1 Analysis of the local distortions

The mass distribution in a cluster of galaxies can be modelled as the linear sum of a global smooth potential (on scales larger than 20 arcsec) and perturbing mass distributions which can then be associated with individual galaxies (with a scalelength less than 20 arcsec). Formally we write the global potential as

$$\phi_{\rm tot} = \phi_{\rm c} + \Sigma_i\, \phi_{{\rm p}_i}, \tag{1}$$

where $\phi_{\rm c}$ is the smooth potential of the cluster and $\phi_{{\rm p}_i}$ are the potentials of the perturbers (galaxy haloes). Henceforth, the subscripts c and p refer to quantities computed for the cluster-scale component and the perturbers respectively. The deflection angle is then given by

$$\theta_{\rm S} = \theta_{\rm I} - \alpha_{\rm I}(\theta_{\rm I})\ ;\ \alpha_{\rm I} = \nabla\phi_{\rm c} + \Sigma_i\, \nabla\phi_{{\rm p}_i}, \tag{2}$$

where $\theta_{\rm I}$ is the angular position of the image and $\theta_{\rm S}$ the angular position of the source. The amplification matrix at any given point is

$$\mathbf{A}^{-1} = \mathbf{I} - \nabla\nabla\phi_{\rm c} - \Sigma_i\, \nabla\nabla\phi_{{\rm p}_i}. \tag{3}$$

Defining the generic symmetry matrix,

$$\mathbf{J}_{2\theta} = \begin{pmatrix} \cos 2\theta & \sin 2\theta \\ \sin 2\theta & -\cos 2\theta \end{pmatrix},$$

we decompose the amplification matrix as a linear sum:

$$\mathbf{A}^{-1} = (1 - \kappa_{\rm c} - \Sigma_i \kappa_{\rm p})\,\mathbf{I} - \gamma_{\rm c} J_{2\theta_{\rm c}} - \Sigma_i\, \gamma_{{\rm p}_i} J_{2\theta_{{\rm p}_i}}, \tag{4}$$

where κ is the magnification and γ the shear. In this framework, the shear γ is taken to be a complex number and is used to define the quantity $\overline{g}$ as follows:

$$\overline{g_{\rm pot}} = \frac{\overline{\gamma}}{1-\kappa} = \frac{\overline{\gamma}_{\rm c} + \Sigma_i\, \overline{\gamma}_{{\rm p}_i}}{1 - \kappa_{\rm c} - \Sigma_i\, \kappa_{{\rm p}_i}},\ \overline{\tau_{\rm pot}} = \frac{2\overline{g_{\rm pot}}}{1 - \overline{g_{\rm pot}}^{*}\overline{g_{\rm pot}}}, \tag{5}$$

which simplifies in the frame of the perturber j to (neglecting the effect of perturber i if $i \neq j$)

$$\overline{g}_{\rm pot}|_j = \frac{\overline{\gamma}_{\rm c} + \overline{\gamma}_{{\rm p}_j}}{1 - \kappa_{\rm c} - \kappa_{{\rm p}_j}}, \tag{6}$$

where $\overline{g}_{\rm pot}|_j$ is the total complex shear induced by the smooth cluster potential and the potentials of the perturbers. Restricting our analysis to the weak regime, and thereby retaining only the first-order terms from the lensing equation for the shape parameters (see Kneib et al. 1996), we have

$$\overline{\tau}_{\rm I} = \overline{\tau}_{\rm S} + \overline{\tau}_{\rm pot}, \tag{7}$$

where $\overline{\tau}_{\rm I}$ is the distortion of the image, $\overline{\tau}_{\rm S}$ is the intrinsic shape of the source, $\overline{\tau}_{\rm pot}$ is the distortion induced by the lensing potentials or, explicitly in terms of $\overline{g}_{\rm pot}$ in the frame of perturber j,

$$\overline{g}_{\rm I} = \overline{g}_{\rm S} + \overline{g}_{\rm pot}|_j = \overline{g}_{\rm S} + \frac{\overline{\gamma}_{\rm c}}{1 - \kappa_{\rm c} - \kappa_{{\rm p}_j}} + \frac{\overline{\gamma}_{{\rm p}_j}}{1 - \kappa_{\rm c} - \kappa_{{\rm p}_j}}. \tag{8}$$

In the local frame of reference of the perturbers, the mean value of the quantity $\overline{g}_{\rm I}$ and its dispersion can be computed in circular annuli (of radius r from the perturber centre) *strictly in the weak regime*,

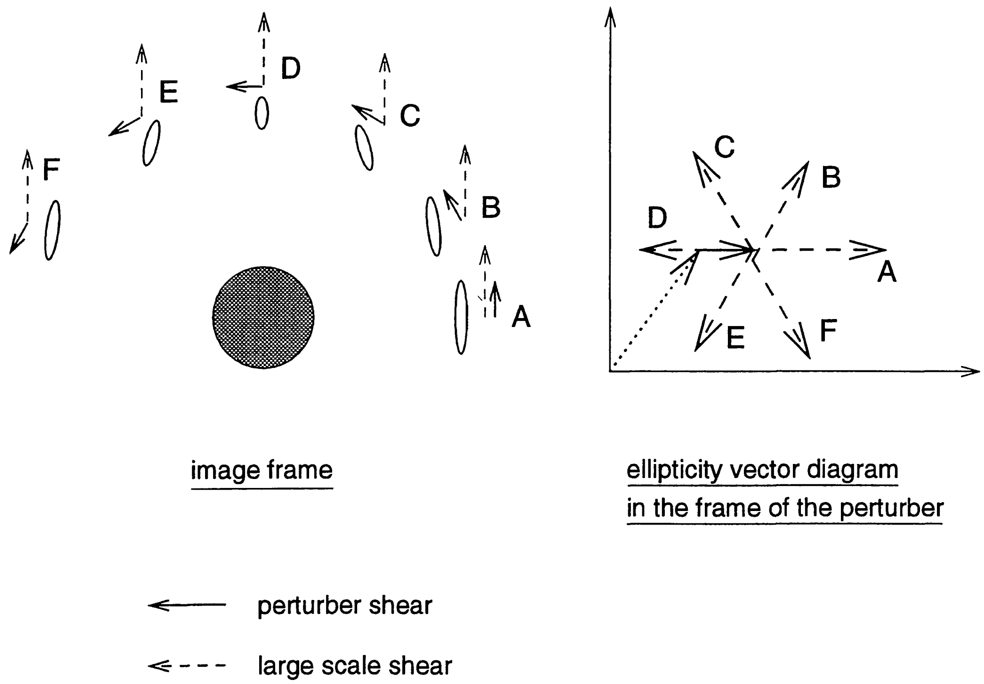

Figure 1. Local frame of reference of the perturber: the vector diagram illustrating the choice of coordinate system. The total shear is decomposed into a large-scale component due to the smooth cluster and a small-scale one due to the perturbing galaxy. In the frame of the perturber, the averaging procedure allows efficient subtraction of the large-scale component as shown in the right panel, enabling the extraction of the shear component induced in the background galaxies only by the perturber as shown in the left panel. The background galaxies (shown in the left panel of this figure) are assumed to have the same intrinsic ellipticity for simplicity, therefore we plot only the induced components.

assuming a constant value $\gamma_c e^{i\theta_{c0}}$ for the smooth cluster component over the area of integration (see Fig. 1 and Fig. 2 for the schematic diagrams).

The result of the integration does depend on the choice of coordinate system. In Cartesian coordinates (averaging out the contribution of the perturbers)

$$\langle \bar{g}_I \rangle_{xy} = \langle \bar{g}_S \rangle + \left\langle \frac{\gamma_c e^{i\theta_{c0}}}{1-\kappa_c-\kappa_{p_j}} \right\rangle + \left\langle \frac{\bar{\gamma}_{p_j}}{1-\kappa_c-\kappa_{p_j}} \right\rangle$$

$$= \gamma_c e^{i\theta_{c0}} \left\langle \frac{1}{1-\kappa_c-\kappa_{p_j}} \right\rangle \equiv \bar{g}_c, \tag{9}$$

$$\sigma^2_{\bar{g}_I} = \frac{\sigma^2_{\bar{g}_S}}{2} + \frac{\sigma^2_{\bar{g}_{p_j}}}{2}, \tag{10}$$

where

$$\sigma^2_{g_I} \approx \frac{\sigma^2_{p(\tau_S)}}{2N_{bg}} + \frac{\sigma^2_{\bar{g}_{p_j}}}{2N_{bg}} \approx \frac{\sigma^2_{p(\tau_S)}}{2N_{bg}}, \tag{11}$$

$\sigma^2_{p(\tau_S)}$ being the width of the intrinsic ellipticity distribution of the sources, N_{bg} the number of background galaxies averaged over and $\sigma^2_{\bar{g}_{p_j}}$ the dispersion due to perturber effects which should be smaller than the width of the intrinsic ellipticity distribution. In the polar *uv* coordinates, on averaging out the smooth part,

$$\langle \bar{g}_I \rangle_{uv} = \langle \bar{g}_S \rangle + \left\langle \frac{\bar{\gamma}_c}{1-\kappa_c-\kappa_{p_j}} \right\rangle + \left\langle \frac{\gamma_{p_j}}{1-\kappa_c-\kappa_{p_j}} \right\rangle$$

$$= \gamma_{p_j} \left\langle \frac{1}{1-\kappa_c-\kappa_{p_j}} \right\rangle \equiv g_{p_j}, \tag{12}$$

$$(\sigma^2_{\bar{g}_I})_{uv} = \frac{\sigma^2_{\bar{g}_S}}{2} + \frac{\sigma^2_{\bar{g}_c}}{2}, \tag{13}$$

where

$$\sigma^2_{g_I} \approx \frac{\sigma^2_{p(\tau_S)}}{2N_{bg}} + \frac{\sigma^2_{\bar{g}_c}}{2N_{bg}}. \tag{14}$$

From these equations, we clearly see the two effects of the contribution of the smooth cluster component: it boosts the shear induced by the perturber due to the $(\kappa_c + \kappa_{p_j})$ term in the denominator, which becomes non-negligible in the cluster centre, and it simultaneously dilutes the regular galaxy–galaxy lensing signal due to the $\sigma^2_{\bar{g}_c}/2$ term (equation 11) in the dispersion of the polarization measure. However, one can in principle optimize the noise in the polarization by 'subtracting' the measured cluster signal and averaging it in polar coordinates:

$$\langle \bar{g}_I - \bar{g}_c \rangle_{uv} = \left\langle \frac{\gamma_{p_j}}{1-\kappa_c-\kappa_{p_j}} \right\rangle, \tag{15}$$

which gives the same mean value as in equation (11) but with a reduced dispersion:

$$(\sigma^2_{\bar{g}_I - \bar{g}_c})_{uv} = \frac{\sigma^2_{\bar{g}_S}}{2}, \tag{16}$$

where

$$\sigma^2_{g_S} \approx \frac{\sigma^2_{p(\tau_S)}}{2N_{bg}}. \tag{17}$$

This subtraction of the larger-scale component reduces the noise in the polarization measure, by about a factor of 2, when $\sigma^2_{\bar{g}_S} \sim \sigma^2_{\bar{g}_c}$, which is the case in cluster cores. Note that in subsequent sections of the paper, we plot the averaged components of $\bar{\tau}$ (the quantity measurable from lensing observations) computed in the *u,v* frame. We reiterate here that the calculations above assume that the cluster

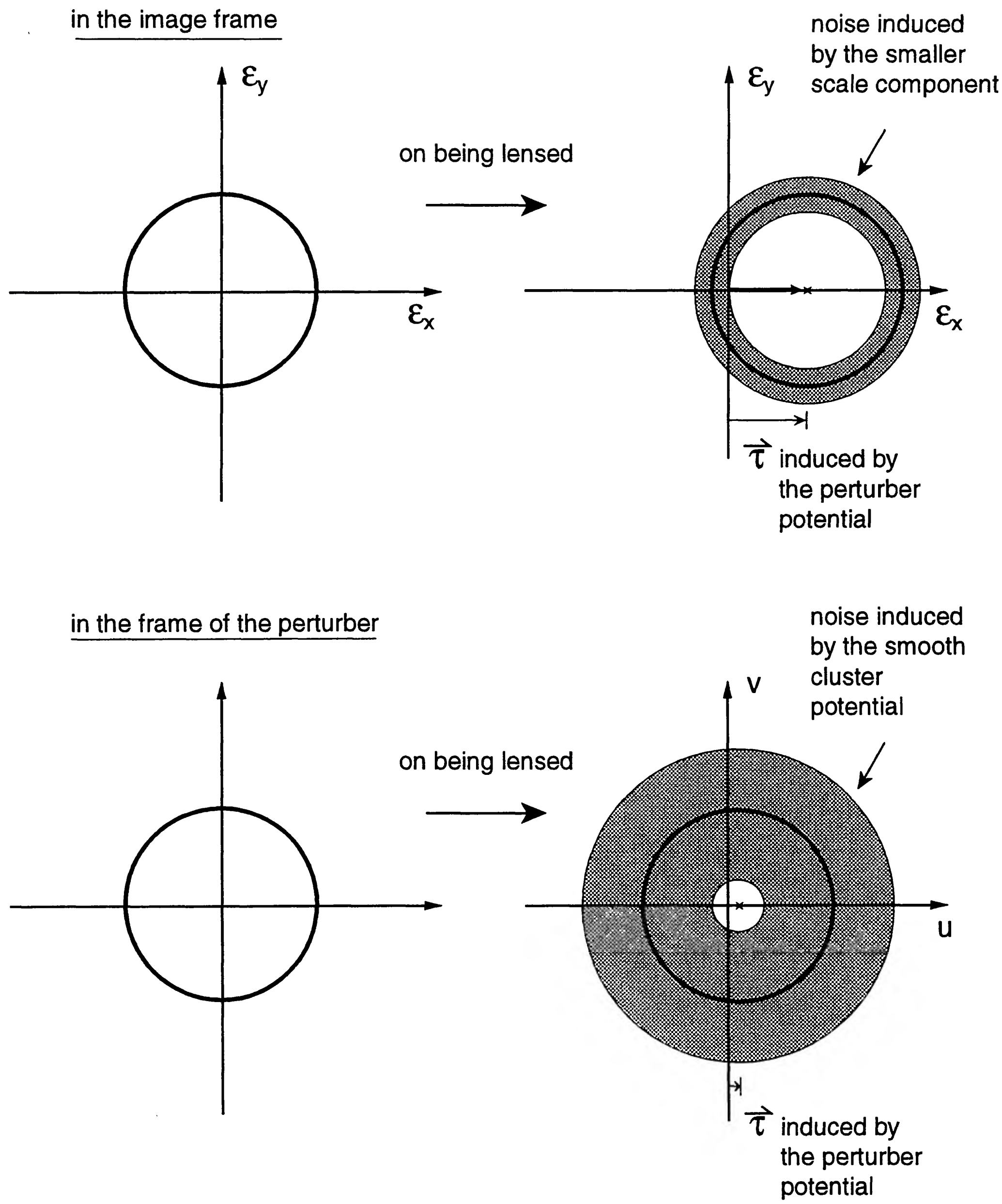

Figure 2. A schematic representation of the effect of the cluster on the intrinsic ellipticity distribution of background sources as viewed from the two different frames of reference. In the top panel – as viewed in the image frame – the effect of the cluster is to cause a coherent displacement τ and the presence of perturbers merely adds small-scale noise to the observed ellipticity distribution. In the bottom panel – as viewed in the perturber frame – the perturber component causes a small displacement τ and the cluster component induces the additional noise.

component is constant over the area of integration (a reasonable assumption if we limit our analysis to small radii around the centres of perturbers). These results can be easily extended to the case when the cluster component is linear over the area of integration, the likely case outside the core region. This direct averaging prescription for extracting the distortions induced by the possible presence of dark haloes around cluster galaxies, by construction, does not require precise knowledge of the centre of the cluster potential well.

2.2 Quantifying the lensing distortion

To quantify the lensing distortion induced by the individual galactic-scale components using a minimal number of parameters to characterize cluster galaxy haloes, we model the density profile as a linear superposition of two pseudo-isothermal elliptical components (PIEMD models derived by Kassiola & Kovner 1993):

$$\Sigma(R) = \frac{\Sigma_0 r_0}{1 - r_0/r_t}\left(\frac{1}{\sqrt{r_0^2 + R^2}} - \frac{1}{\sqrt{r_t^2 + R^2}}\right), \tag{18}$$

with a model core radius r_0 and a truncation radius $r_t \gg r_0$. The useful feature of this model is the ability to reproduce a large range of mass distributions by varying only the ratio η, defined as $\eta = r_t/r_0$. It also provides the following simple relation between the truncation radius and the effective radius R_e: $r_t \sim (4/3)R_e$. Furthermore, this apparently circular model can be easily generalized to the elliptical case by re-defining the radial coordinate R as follows:

$$R^2 = \left[\frac{x^2}{(1+\epsilon)^2} + \frac{y^2}{(1-\epsilon)^2}\right]; \quad \epsilon = \frac{a-b}{a+b}. \tag{19}$$

The mass enclosed within radius R for the model is given by

$$M(R) = \frac{2\pi\Sigma_0 r_0}{1 - \frac{r_0}{r_t}}\left[\sqrt{r_0^2+R^2} - \sqrt{r_t^2+R^2} + (r_t - r_0)\right], \tag{20}$$

and the total mass, which is finite, is

$$M_\infty = 2\pi\Sigma_0 r_0 r_t. \tag{21}$$

Calculating κ, γ and g, we have

$$\kappa(R) = \kappa_0 \frac{r_0}{(1 - r_0/r_t)}\left[\frac{1}{\sqrt{(r_0^2+R^2)}} - \frac{1}{\sqrt{(r_t^2+R^2)}}\right], \tag{22}$$

$$2\kappa_0 = \Sigma_0 \frac{4\pi G}{c^2}\frac{D_{ls}D_{ol}}{D_{os}}, \tag{23}$$

where D_{ls}, D_{os} and D_{ol} are respectively the lens–source, observer–source and observer–lens angular diameter distances. To obtain $g(R)$, knowing the magnification $\kappa(R)$, we solve Laplace's equation for the projected potential ϕ_{2D}, evaluate the components of the amplification matrix and then proceed to solve directly for $\gamma(R)$, $g(R)$ and $\tau(R)$:

$$\phi_{2D} = 2\kappa_0\Bigg[\sqrt{r_0^2+R^2} - \sqrt{r_t^2+R^2} + (r_0 - r_t)\ln R - r_0\ln\left(r_0^2 + r_0\sqrt{r_0^2+R^2}\right) + r_t\ln\left(r_t^2 + r_t\sqrt{r_t^2+R^2}\right)\Bigg]. \tag{24}$$

To first approximation,

$$\tau(R) \approx \gamma(R) = \kappa_0\left[-\frac{1}{\sqrt{R^2+r_0^2}} + \frac{2}{R^2}\left(\sqrt{R^2+r_0^2} - r_0\right) + \frac{1}{\sqrt{R^2+r_t^2}} - \frac{2}{R^2}\left(\sqrt{R^2+r_t^2} - r_t\right)\right]. \tag{25}$$

Scaling this relation by r_t gives, for $r_0 < R < r_t$,

$$\gamma(R/r_t) \propto \frac{\Sigma_0}{\eta - 1}\frac{r_t}{R} \sim \frac{\sigma^2}{R}, \tag{26}$$

where σ is the velocity dispersion, and, for $r_0 < r_t < R$,

$$\gamma(R/r_t) \propto \frac{\Sigma_0}{\eta}\frac{{r_t}^2}{R^2} \sim \frac{M_{tot}}{R^2}, \tag{27}$$

where M_{tot} is the total mass. In the limit that $R \gg r_t$, we have

$$\gamma(R) = \frac{3\kappa_0}{2R^3}(r_0^2 - r_t^2) + \frac{2\kappa_0}{R^2}(r_t - r_0), \tag{28}$$

and, as $R \to \infty$, $\gamma(R) \to 0$, $g(R) \to 0$ and $\tau(R) \to 0$ as expected.

3 RECOVERING GALACTIC-SCALE PERTURBATIONS

In this section, we study the influence of the various parameters using the direct averaging procedure on the synthetic data obtained from simulations. The numerical simulations involve modelling of the global cluster potential and the individual perturbing cluster galaxies, and calculating their combined lensing effects on a catalogue of faint galaxies. We compute the mapping between the source and image plane and hence solve the lensing equation, using the lens tool utility developed by Kneib (1993), which accounts consistently for the displacement and distortion of images in both the strong and weak lensing regimes.

3.1 Modelling the cluster galaxies

3.1.1 Spatial and luminosity distribution

A catalogue of cluster galaxies was generated at random with the following characteristics. The luminosities were drawn from a standard Schechter function with $L_* = 3\times10^{10}\,L_\odot$ and $\alpha = -1.25$. The positions were assigned consistently with the number density $\nu(r)$ of a modified Hubble law profile,

$$\nu(r) = \frac{\nu_0}{\left(1 + \frac{r^2}{r_0^2}\right)^{1.5}}, \tag{29}$$

with a core radius $r_0 = 250$ kpc, as well as a more generic 'core-less' profile of the form

$$\nu(r) = \frac{\nu_0}{\left(\frac{r}{r_s}\right)^\alpha\left(1 + \frac{r^2}{r_s^2}\right)^{2-\alpha}} \tag{30}$$

with a scale-radius $r_s = 200$ kpc and $\alpha = 0.1$ which was found to be a good fit to the galaxy data of the moderate-redshift lensing cluster A2218 by Natarajan & Kneib (1996). We find however, that the results for the predicted shear from the simulations are independent of this choice.

3.1.2 Scaling laws

The individual galaxies are then parametrized by the mass model of Section 2.2, using in addition the following scalings with luminosity (see Brainerd et al. 1996 for an analogous treatment) for the central velocity dispersion σ_0, the truncation radius r_t and the core radius r_0:

$$\sigma_0 = \sigma_{0*}\left(\frac{L}{L_*}\right)^{\frac{1}{4}}; \tag{31}$$

$$r_0 = r_{0*}\left(\frac{L}{L_*}\right)^{\frac{1}{2}}; \tag{32}$$

$$r_t = r_{t*}\left(\frac{L}{L_*}\right)^{\alpha}. \tag{33}$$

These imply the following scaling for the r_t/r_0 ratio η:

$$\eta = \frac{r_t}{r_0} = \frac{r_{t*}}{r_{0*}}\left(\frac{L}{L_*}\right)^{\alpha - 1/2}. \tag{34}$$

The total mass M then scales with the luminosity as

$$M = 2\pi\Sigma_0 r_0 r_t = \frac{9}{2G}(\sigma_0)^2 r_t = \frac{9}{2G}{\sigma_{0*}}^2 r_{t*}\left(\frac{L}{L_*}\right)^{\frac{1}{2}+\alpha}, \tag{35}$$

where α tunes the size of the galaxy halo, and the mass-to-light ratio Υ is given by

$$\Upsilon = 12\left(\frac{\sigma_{0*}}{240\,\mathrm{km\,s^{-1}}}\right)^2\left(\frac{r_{t*}}{30\,\mathrm{kpc}}\right)\left(\frac{L}{L_*}\right)^{\alpha-1/2}. \tag{36}$$

Therefore, for $\alpha = 0.5$ the assumed galaxy model has constant Υ for each galaxy; if $\alpha > 0.5$ ($\alpha < 0.5$) then brighter galaxies have larger (smaller) haloes than the fainter ones.

The physical motivation for exploring these scaling laws arises from trying to understand the observed empirical correlations for early-type (E and S0) galaxies in the Fundamental Plane (FP). The following tight relation between the effective radius R_e, the central

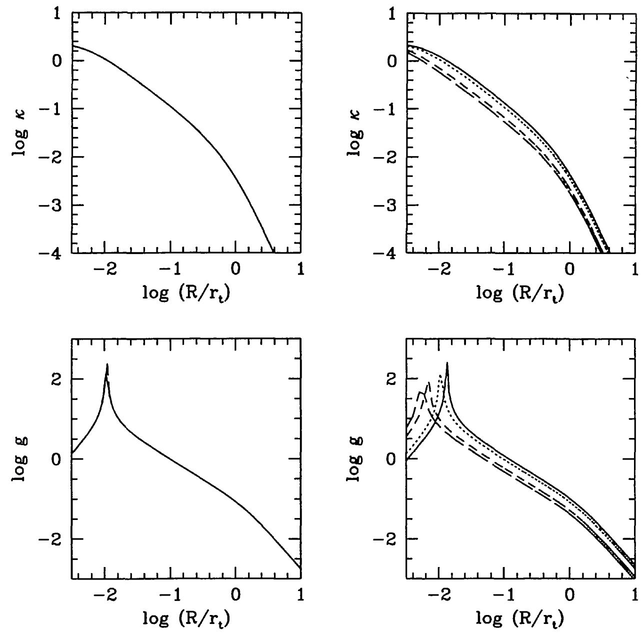

Figure 3. The effects of the assumed scaling relations are examined in a plot of the magnification log κ versus $\log(R/r_t)$ and the shear $\log g$ versus $\log(R/r_t)$ for various values of (L/L^*): 0.5, 1.0, 5.0 and 10.0. The curves in the left panels are for $\alpha = 0.5$ and those in the right panels for $\alpha = 0.8$. (i) Solid curves – $(L/L^*) = 0.5$, (ii) dotted curves – $(L/L^*) = 1.0$, (iii) short-dashed curves – $(L/L^*) = 5.0$, (iv) long-dashed curves – $(L/L^*) = 10$. The magnification is normalized so that at $r = 2\ r_0$, $\kappa = 1$; the difference in the slope of κ above and below $\log(r/r_t) = 0$ can be clearly seen for both sets of scaling laws. Note that a spike appears in the plots of $\log g$ versus $\log(R/r_t)$ at the radius where the mean enclosed surface density is approximately equal to the critical surface density. For the mass models studied here (cuspy with small core-radii) the surface mass density has a large central value and hence a spike appears on a scale that is roughly comparable to the core-radius.

velocity dispersion σ_0 and the mean surface brightness within R_e is found for cluster galaxies (Jorgensen, Franx & Kjaergaard 1996; Djorgovski & Davis 1987; Dressler et al. 1987):

$$\log R_e = 1.24 \log \sigma_0 - 0.82 \log \langle I \rangle_e + \text{constant}. \quad (37)$$

One of the important consequences of this relation is the fact that it necessarily implies that the mass-to-light ratio is a weak function of the luminosity, typically $\Upsilon \sim L^{0.3}$ (Jorgensen et al. 1996). In terms of our scaling laws, this implies $\alpha = 0.8$. Henceforth, in this analysis we explore both the scaling relations: for $\alpha = 0.5$, the constant mass-to-light ratio case; and $\alpha = 0.8$, corresponding to the mass-to-light ratio being proportional to $L^{0.3}$– consistent with the observed FP. In Fig. 3, we plot the scaling relations for various values of (L/L_*), ranging from 0.5 to 10.0 for $\alpha = 0.5$ and $\alpha = 0.8$. Additionally, for the constant mass-to-light ratio case, we also plot the iso-Υ curves in terms of the fiducial σ_0^* and r_{t^*} in Fig. 4. The scaling laws are calibrated by defining an L_* (in the R band) elliptical galaxy to have $r_{0*} = 0.15$ kpc, $r_{t*} = 30.0$ kpc and a fiducial σ_{0*}, then chosen to assign the different mass-to-light ratios [$\sigma_{0*} = 100$, 140, 170, 240, 340, 480 km s^{-1} corresponding to $\Upsilon = 2$, 4, 6, 12, 24, 48 respectively].

3.2 Modelling the background galaxies

3.2.1 Luminosity distribution

The magnitude and hence the luminosity for the background population were generated consistently with the number count

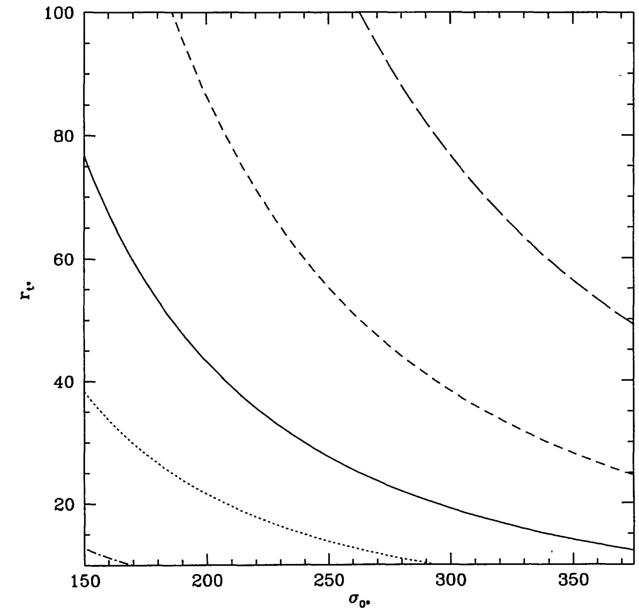

Figure 4. The constant mass-to-light ratio curves are plotted in the (σ_{0*}, r_t^*) plane for an L_* galaxy with $\eta = 200$: (i) dot-dashed curve – $\Upsilon = 4$, (ii) dotted curve – $\Upsilon = 6$, (iii) solid curve – $\Upsilon = 12$, (iv) short-dashed curve – $\Upsilon = 24$ and (v) long-dashed curve – $\Upsilon = 48$.

distribution measured from faint field galaxy surveys like the MDS as reported in Glazebrook et al. (1994), as well as the more recent results of the number–magnitude relations obtained from the *Hubble Deep Field* data (Abraham et al. 1996). The slope of the number count distribution used was 0.33 over the magnitude range $m_R = 18 - 26$. This power law for the number counts implies a surface number density that is roughly 90 galaxies per square arcminute in the given magnitude range (see Smail et al. 1995b), which over the area of the simulation frame [8×8 arcmin^2] corresponds to having $\sim$ 5000 background galaxies.

3.2.2 Redshift distribution

The background galaxy population of sources was also generated, consistently with the measured redshift, magnitude and luminosity distributions (Model Z2 below), from high-redshift surveys like the APM and CFRS (Efstathiou et al. 1991 and Lilly et al. 1995 respectively). For the normalized redshift distribution at a given magnitude m (in the R band) we used the following fiducial forms.

Model Z1:

$$N(z, m) = N_0 \delta(z - 2), \quad (38)$$

corresponding to the simple case of placing all the sources at $z = 2$.

Model Z2:

$$N(z, m) = \frac{\beta \left(\frac{z^2}{z_0^2}\right) \exp\left[-\left(\frac{z}{z_0}\right)^{\beta}\right]}{\Gamma\left(\frac{3}{\beta}\right) z_0}, \quad (39)$$

where $\beta = 1.5$ and

$$z_0 = 0.7 \left[z_{\rm median} + \frac{{\rm d}z_{\rm median}}{{\rm d}m_R} (m_R - m_{R0}) \right], \quad (40)$$

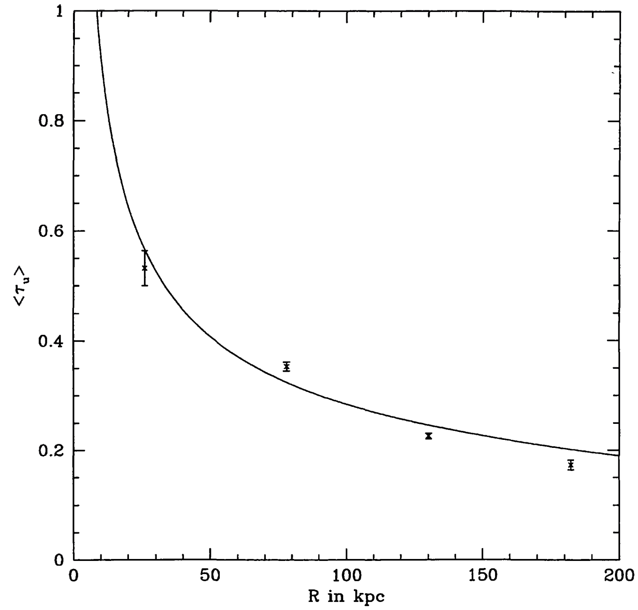

Figure 5. Demonstrating the robustness of the signal extraction by comparing the analytic prediction with the measured radially averaged shear from the simulation. The signal was extracted from a simulation run of a PIEMD model with $r_{t*} = 30$ kpc, $r_{0*} = 0.15$ kpc and a velocity dispersion of 480 kms^{-1}: the solid curve shows the estimate from the analytic formula and overplotted are the measured values of the averaged shear.

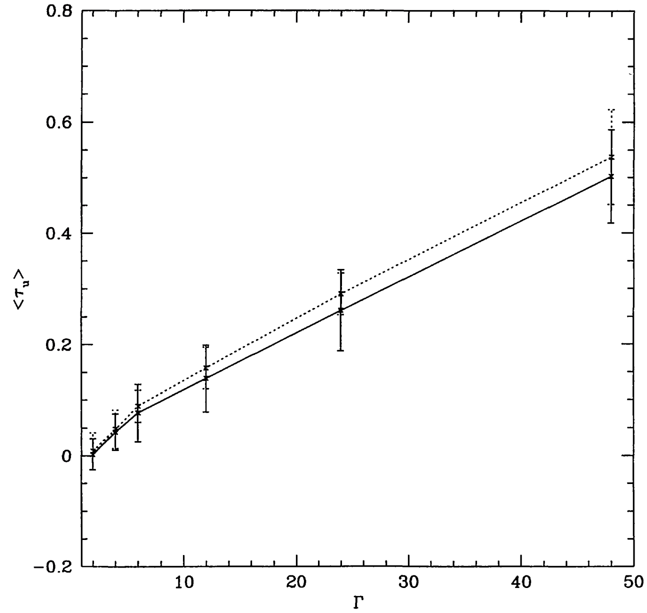

Figure 6. Variation of the mean value of the signal in the first annulus with mass-to-light ratio Υ: for Υ= 2, 4, 6, 12, 24, 48; the cluster galaxies are plotted for Model Z1 (solid curve) and Model Z2 (dotted curve).

$z_{\rm median}$ being the median redshift, $dz_{\rm median}/dm_R$ the change in median redshift with R magnitude m_R. We use for our simulations m_{R0} =22.0, $dz_{\rm median}/dm_R$=0.1 and $z_{\rm median}$= 0.58 [see Brainerd et al. (1996) and Kneib et al. (1996)].

3.2.3 Ellipticity distribution

Analysis of deep surveys such as the MDS fields (Griffiths et al. 1994) shows that the ellipticity distribution of sources is a strong function of the sizes of individual galaxies as well as their magnitude (Kneib et al. 1996). For the purposes of our simulations, since we assume 'perfect seeing', these effects are ignored and the ellipticities are assigned in accordance with the ellipticity distribution $p(\tau_S)$ derived from fits to the MDS data (Ebbels, Kneib & Ellis, in preparation) of the form

$$p(\tau_S) = \tau_S \exp\left[-\left(\frac{\tau_S}{\delta}\right)^\alpha\right]; \ \alpha = 1.15, \ \delta = 0.25. \qquad (41)$$

4 ANALYSIS OF THE SIMULATIONS

We use the above as input distributions to simulate the background galaxies and bright cluster galaxies in addition to a model for the cluster-scale mass distribution. Analogous to the mass model constructed for the cluster Abell 2218 (Kneib et al. 1996), we set up an elliptical mass distribution for the central clump with a velocity dispersion of 1100 km s^{-1} placed at a redshift $z = 0.175$. The main clump was modelled using a PIEMD profile (as in equation 14) with an ellipticity $\epsilon = 0.3$, a core radius 70 kpc and a truncation radius 700 kpc; therefore the surface mass density of the clump falls off as r^{-3} for $r \gg r_t$.

The lens equation was then solved for the specified configurations of sources and lenses set up as above and the corresponding image frames were generated. The averaged components of the shear binned in circular annuli centred on the perturbing galaxies were evaluated in their respective local (u, v) frames. An important check on the entire recovery procedure arises from the fact that by construction [choice of the (u, v) coordinate system] the mean value of the v-component of the shear $< \tau_v >$ is required to vanish.

In the following subsections, we explore the dependence of the strength of the detected signal on the various input parameters. First of all, Fig. 5 demonstrates the good agreement between the analytic formula for the shear derived at a given radial distance R produced by a PIEMD model as computed in Section 2.2 and the averaged value extracted from the simulation on solving the lensing equation exactly for the redshift distribution of Model Z1. In Fig. 6 the variation of the mean value of the signal in the first annulus is plotted as a function of Υ. In all subsequent plots (Figs 6, 7, 8, 9, 10, 12 and 13) the annuli are scaled such that for an L_* galaxy, the width of each ring corresponds to a physical scale of $\sim$ 20 kpc at $z = 0.175$.

4.1 Error estimate on the signal

There are two principal sources of error in the computation of the averaged value of the shear aside from the observational errors (which are not taken into account in these simulations) arising from the effects of seeing, etc.: (i) shot noise (due to a finite number of sources and the intrinsic width of their ellipticity distribution) and (ii) in principle the unknown source redshifts. Therefore, we require a minimum threshold number of background objects to obtain a significant level of detection. The unknown redshift distribution of the sources also introduces noise and affects the retrieval of the signal in a systematic way: for instance, the obtained absolute value for the total mass estimate for cluster galaxies is an under-estimate for a higher redshift population for a given measured value of the shear. The mean (or alternatively the median) and width of the redshift distribution are the important parameters that determine the errors incurred in the extraction procedure.

For the simulation, however, we need to obtain an error estimate on the signal given that we measure the averaged shear for a single realization. In order to do so, the simulation was set up with a

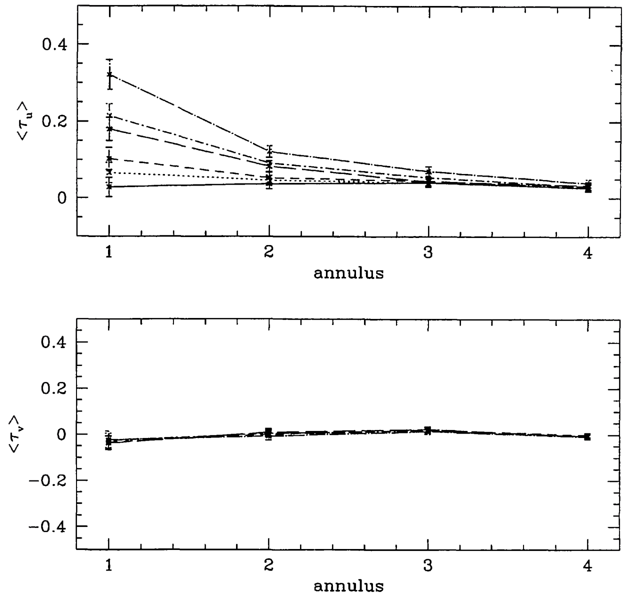

Figure 7. Recovering the signal for Model Z1, for various values of the constant mass-to-light ratio Υ of the cluster galaxies ranging from 2 to 48: (i) lower solid curve – the error estimate, (ii) upper solid curve – $\Upsilon = 2$, (iii) dotted curve – $\Upsilon = 4$, (iv) dashed curve – $\Upsilon = 6$, (v) long-dashed curve – $\Upsilon = 12$, (vi) dot-short-dashed curve – $\Upsilon = 24$, (vii) dot-long-dashed curve – $\Upsilon = 48$. Note here that $< \tau_v >$ is zero as expected by definition of the (u, v) coordinate system.

constant mass-to-light ratio ($\Upsilon = 12$) for the 50 cluster galaxies with 5000 background galaxies, and on solving the lens equation the image frame was obtained. The averaging procedure as outlined in Section 2.1 was then implemented to extract the output signal with 1000 independent sets of random scrambled positions for the cluster galaxies (in addition to the one set of 50 positions that was actually used to generate the image); the results are plotted as the lower solid curves in Figs 7 and 8. This is a secure estimate of the error arising for an individual realization, since this error arises primarily from the dilution of the strength of the measured shear due to uncorrelated sources and lensed images. We found that the mean error in $\langle \tau_u \rangle$ in the first annulus is 0.040 ± 0.0012 and the error in $\langle \tau_v \rangle$ is 0.0048 ± 0.0047.

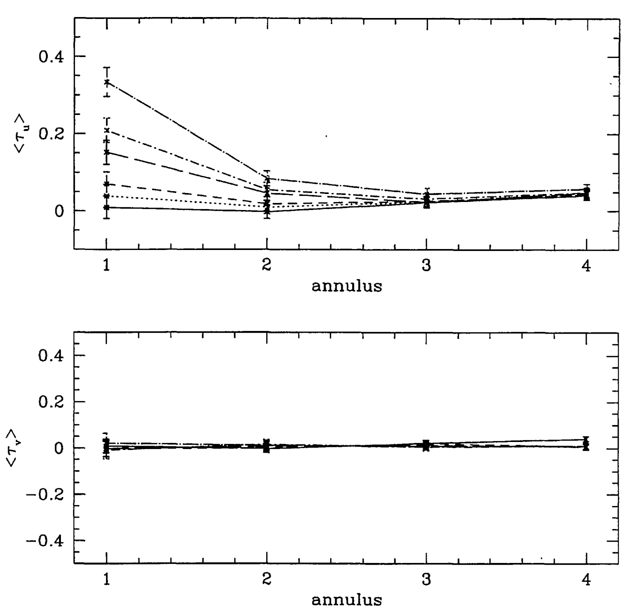

Figure 8. Recovering the signal for Model Z2, for various values of the constant mass-to-light ratio Υ of the cluster galaxies ranging from 2 to 48: (i) lower solid curve – the error estimate, (ii) upper solid curve – $\Upsilon = 2$, (iii) dotted curve – $\Upsilon = 4$, (iv) dashed curve – $\Upsilon = 6$, (v) long-dashed curve – $\Upsilon = 12$, (vi) dot-short-dashed curve – $\Upsilon = 24$, (vii) dot-long-dashed curve – $\Upsilon = 48$.

4.2 Variation of the signal with mass-to-light ratio of cluster galaxies

The simulations were performed for mass-to-light ratios (Υ) ranging from 2 to 48 (see Figs 6, 7 and 8). The velocity dispersion of the fiducial galaxy model was adjusted to give the requisite value for Υ, keeping the scaling relations intact. The detection is significant for mass-to-light ratios $\Upsilon \geq 4$ given the configuration with 50 cluster galaxies and 5000 background galaxies. The strength of the signal varies with the input Υ of the cluster galaxies, and increases with increasing Υ. As a test run, with $\Upsilon = 0$ (i.e. no cluster galaxies) and only the large-scale component of the shear, we do recover the expected behavior for $\langle \tau_u \rangle$. The signal was extracted for both background source redshift distributions Model Z1 and Model Z2. While the amplitude of the signal is not very sensitive to the details of the redshift distribution of the background population and hence did not vary significantly, the error-bars are marginally larger for Model Z2. This can be understood in terms of the additional shot noise induced due to the change in the relative number of objects 'available' for lensing: in Model Z2 a fraction of the galaxies in the low-z tail of the redshift distribution end up as foreground objects and are hence not lensed, thereby diluting the signal and increasing the size of the error-bars marginally.

4.3 Variation with the number of background galaxies

The efficiency of detection of the signal depends primarily on the number of background galaxies averaged over in each annulus, and therefore on the number that are lensed by the individual cluster galaxies. For a fixed value of Υ, the total number of background galaxies $N_{\rm bg}$ was varied, assuming a redshift distribution of the form of Model Z1. With increasing $N_{\rm bg}$, $1000 \rightarrow 2500 \rightarrow 5000$, the detection is more secure and the error does vary roughly as $\sqrt{N_{\rm bg}}$ as shown in Fig. 9. In principle, the larger the number of background sources available for lensing, the more significant the detection with tighter error bars; however, we find that a ratio of 50 cluster galaxies to 2500 background galaxies provides a secure detection for $\Upsilon \geq 4$, while a larger number of background sources are required to detect the corresponding signal induced by lower mass-to-light ratio haloes. A secure detection in this case refers to the fact that the difference in the mean values of the detected signal in the two cases (with $N_{\rm bg} = 5000$ and $N_{\rm bg} = 2500$ background sources) is comparable to the mean estimated error per realization computed in Section 4.1. The number count distribution used to generate the background sources corresponds to a background surface number density of ~ 90 galaxies per square arcmin which we find provides a secure detection for $\Upsilon \geq 4$. It is useful to point out here that for the standard Bruzual & Charlot (95) spectral evolution of stellar population synthesis models with solar metallicity, and a galaxy that is roughly 10 Gyr old (a reasonable age estimate for a galaxy in a $z \sim 0.3$ cluster), formed in a single 1-Gyr burst of star formation and having evolved passively, one obtains a stellar mass-to-light ratio in the R band of ~ 8 with a single-power-law Salpeter initial mass function (IMF) with a lower mass limit of 0.1 $M_\odot$ and an upper

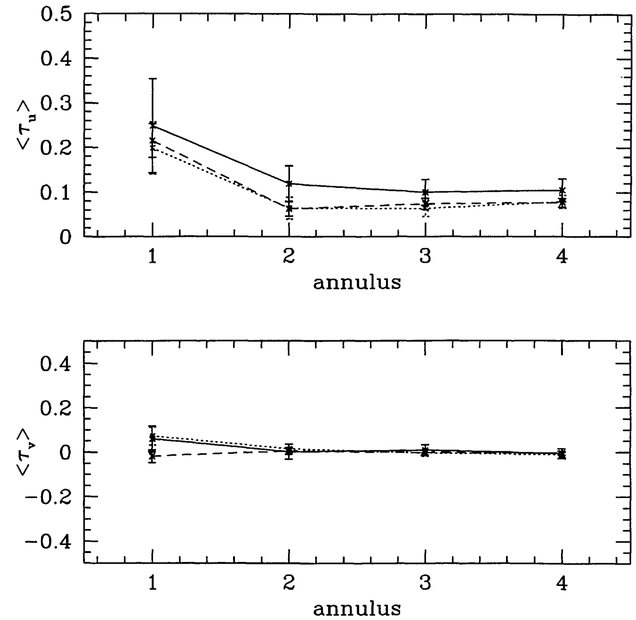

Figure 9. Variation of the signal with the number of background galaxies for Model Z1: for a given mass-to-light ratio Υ= 12 of the cluster galaxies. We find that the error bars and hence the noise decrease as expected with increasing $N_{\rm bg}$: (i) solid curve $N_{\rm bg}$ = 1000, (ii) dashed curve $N_{\rm bg}$ = 2500, (iii) dotted curve $N_{\rm bg}$ = 5000.

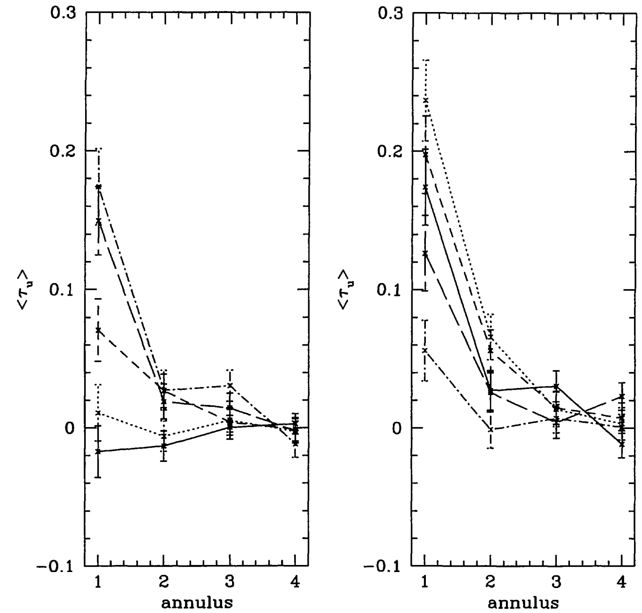

Figure 11. Variation of the signal with cluster redshift for Model Z2: for a given constant mass-to-light ratio Υ= 12 of the cluster galaxies, placing the lens at different redshifts. Right panel: (i) solid curve z = 0.1, (ii) dotted curve z = 0.2, (iii) dashed curve z = 0.3, (iv) long-dashed curve z = 0.4, (v) dot-dashed curve z = 0.5. Left panel: (i) solid curve z = 0.01, (ii) dotted curve z = 0.02, (iii) dashed curve z = 0.05, (iv) long-dashed curve z = 0.07, (v) dot-dashed curve z = 0.10.

mass limit of 125 $M_\odot$. With the same ingredients but a Scalo IMF one obtains a mass-to-light ratio about a factor of 2 smaller (∼4) since there are a smaller proportion of very low-mass stars. Therefore, an R-band mass-to-light ratio of 4 for a cluster galaxy is consistent with the observed mass just in stars and does not imply the presence of any dark mass in the system. Therefore, if dark haloes were indeed present around the bright cluster members, the corresponding inferred mass-to-light ratios would be greater than 4, and with 5000 background galaxies, we would be sensitive to the signal as shown in the plots of Figs 6, 7 and 8.

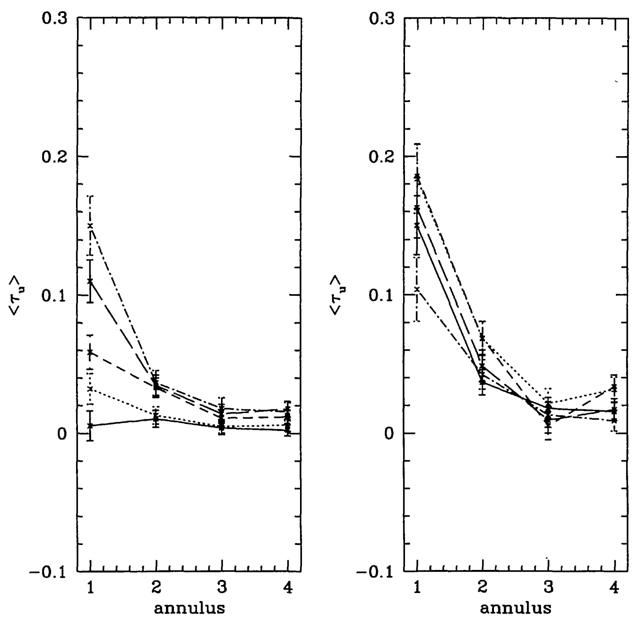

Figure 10. Variation of the signal with cluster redshift for Model Z1: for a given mass-to-light ratio Υ= 12 of the cluster galaxies, placing the lens at different redshifts. Right panel: (i) solid curve z = 0.1, (ii) dotted curve z = 0.2, (iii) dashed curve z = 0.3, (iv) long-dashed curve z = 0.4, (v) dot-dashed curve z = 0.5. Left panel: (i) solid curve z = 0.01, (ii) dotted curve z = 0.02, (iii) dashed curve z = 0.05, (iv) long-dashed curve z = 0.07, (v) dot-dashed curve z = 0.10.

4.4 Variation with cluster redshift

The lensing signal depends on the distance ratio $D_{\rm ls}/D_{\rm os}$, the angular extent of the lensing objects, the number density of faint objects and their redshift distribution. We performed several runs with the cluster (the lens) placed at different redshifts, ranging from z = 0.01 to 0.5. We scaled all the distances with the appropriate factors corresponding to each redshift for both Models Z1 and Z2 (Figs 10–12). For Model Z1 (Fig. 10 and dotted curve in Fig. 12), we find that the signal (by which we refer to the value of $\langle \tau_u \rangle$ in the innermost annulus) saturates at low redshifts; for $0.01 < z_{\rm lens} < 0.07$ the measurements are consistent with no detection but the strength increases as $z_{\rm lens}$ is placed further away and it remains significant for up to $z_{\rm lens} = 0.4$, subsequent to which it falls sharply once again at 0.5. On the other hand, we find that for Model Z2 (Fig. 11, and solid curve in Fig. 12), there is a well-defined peak and hence an optimal lens redshift range for extracting the signal. Thus, in general, cluster lenses lying between redshifts 0.1 and 0.3 are the most suitable ones for constraining the mean Υ of cluster galaxies via this direct averaging procedure. These trends with redshift can be understood easily: the shear produced is proportional to the surface mass density and scales as ($D_{\rm ls}/D_{\rm os}$); the saturation at high redshift is due to the combination of two diluting effects, (i) the decrease in $D_{\rm ls}$ as the lens is placed at successively higher redshifts, and (ii) the effect of additional noise induced due to a reduction in the number of background objects for Model Z2. The drop-off at low z (for both models) is primarily due to the behaviour of the angular scale factors at low redshifts. Additionally, the shape of these curves is

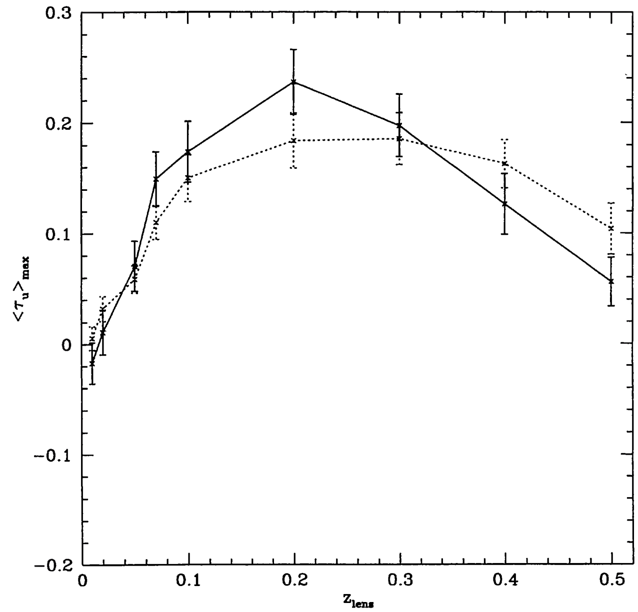

Figure 12. Variation of the maximum value of the signal with redshift: for a given constant mass-to-light ratio $\Upsilon = 12$ of the cluster galaxies, placing the lens at different redshifts for the two background redshift distributions for the sources. (i) Dotted curve: Model Z1; (ii) solid curve: Model Z2.

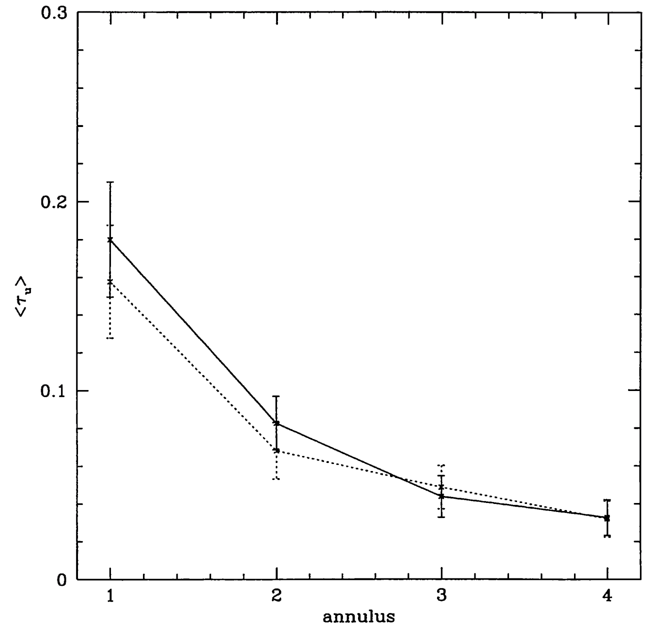

Figure 13. Examining the scaling relations – the two choices of α, the exponent of the scaling relation for the truncation radius, for $\Upsilon = 12$. We plot the recovered signal: (i) solid curve, $\alpha = 0.8$, (ii) dotted curve, $\alpha = 0.5$.

independent of the total mass of the cluster (the total mass being dominated by the smooth component), therefore even for a sub-critical cluster we obtain the same variation with redshift.

4.5 Dependence on assumed scaling laws

In Section 3.1, we outlined the simple scaling relations that were used to model the cluster galaxies. The choice of the exponent α in equation (34) allows the modelling of the trends for different galaxy populations: $\alpha = 0.5$ corresponding to a constant Υ and $\alpha = 0.8$ corresponding to Υ being a weak function of the luminosity. Simulating both these cases, we find that the mean value of the signal does depend on the assumed exponent for the scaling law since it is a measure of the mass enclosed (Fig. 13). We find that the signal is stronger for $\alpha = 0.8$; it is not possible, however, to distinguish between a correspondingly higher value of the constant mass-to-light ratio and a higher value of α. Therefore, the direct averaging procedure cannot discriminate between $\alpha = 0.5$ and $\alpha = 0.8$ which correspond to different detailed fall-offs for the mass distribution.

4.6 Examining the assumption of analysis in the weak regime

While our mathematical formulation outlined in Section 2 is strictly valid only for $\kappa \ll 1$, we examine how crucial this assumption is to the implementation of the technique. For the output images from the simulations, the magnification κ is known at all points. Prior to the averaging, we excised the high-κ regions successively, by removing only the lenses in those regions. The results are plotted in Fig. 14 for input $\Upsilon = 12$, with the sources distributed as specified by Model Z1. While the mean peak value of the signal does not fluctuate much, on removing the high-κ regions, we find that the cluster subtraction does get progressively more efficient, as evidenced by the sharp fall-off to zero of the signal in the second annulus outward. Therefore, while the detectability and magnitude of the signal are robust even in the 'strong regime', the contribution from the smooth cluster component, which for our purposes is a contaminant, can be 'removed' optimally only in the low-κ regions.

5 MAXIMUM LIKELIHOOD ANALYSIS

5.1 Limitations of the direct averaging method

The simulations have enabled us to delineate the role of relevant parameters and comprehend the trends with cluster redshift, the redshift distribution of the sources and the mass-to-light ratio of the

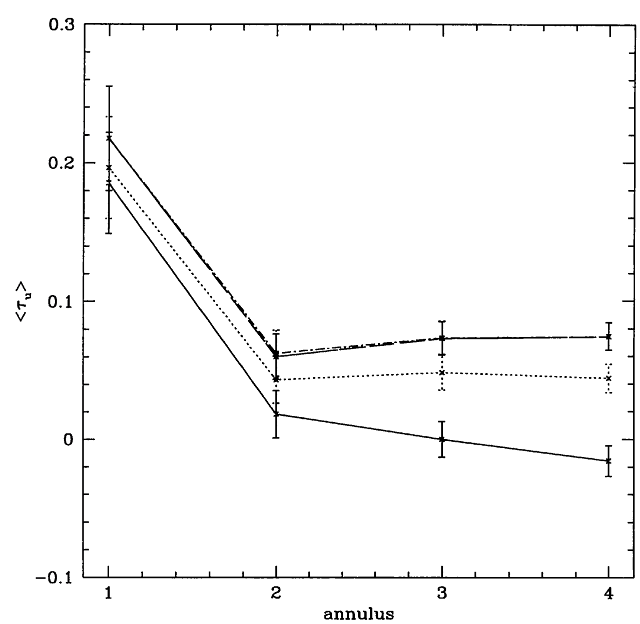

Figure 14. The effect of excising the high-κ regions in the image (for $\Upsilon = 12$ of the cluster galaxies): (i) solid curve, $\kappa \leq 0.1$, (ii) dotted curve, $\kappa \leq 0.2$, (iii) dashed curve, $\kappa \leq 0.3$, (iv) long-dashed curve, $\kappa \leq 0.4$, (v) dot-dashed curve, $\kappa \leq 0.5$.

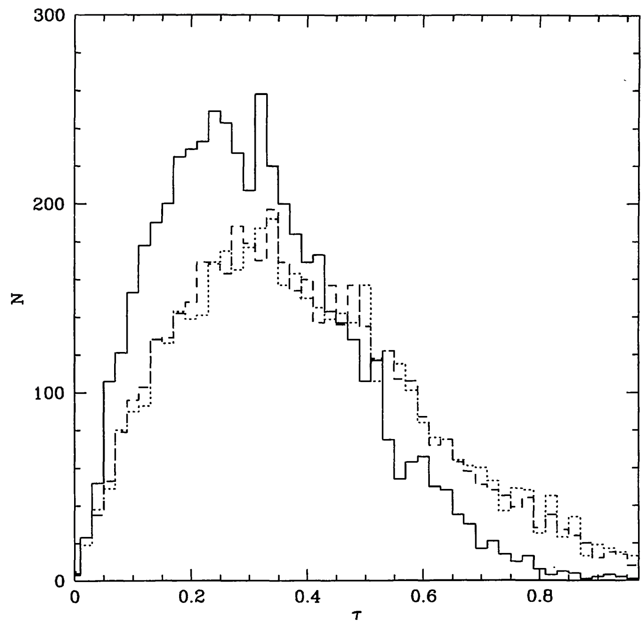

Figure 15. The ellipticity distribution p_{τ_S}: (i) solid curve – intrinsic input ellipticities of the sources, (ii) dotted curve – the ellipticity distribution on being lensed by 50 galactic-scale mass components and one larger-scale smooth component, and (iii) dashed curve – the ellipticity distribution induced by lensing only by the larger-scale smooth cluster component.

cluster galaxies. The direct method suffers from the following limitations, especially in the cluster core: (i) being in the 'strong' lensing regime, the 'cluster subtraction' is not very efficient; and (ii) the probability of a background galaxy being sheared due to the cumulative effect of two or more cluster galaxies is enhanced, the core being a region with a high number density of cluster galaxies. It does, however, provide a robust estimate of the mass-to-light ratio modulo the assumed model parameters.

We now explore application of a maximum likelihood method to obtain significance bounds on fiducial parameters that characterize a 'typical' galaxy halo in the cluster. Schneider & Rix (1996) developed a maximum likelihood prescription for galaxy–galaxy lensing in the field; here we develop one to study lensing by galaxy haloes embedded in the cluster. Schematically, we demonstrate the differences in the ellipticity distribution that we are attempting to discern in Fig. 15. Here we have plotted the intrinsic ellipticity distribution of the unlensed sources, sources lensed only by a cluster-scale component and sources sheared by both a cluster-scale component and 50 cluster galaxies; from this it is obvious that the effect that we intend to measure in terms of parameters that characterize the cluster galaxies is indeed small, hence recovery of the fiducial parameters in this case is considerably harder than in the case of purely galaxy–galaxy lensing.

5.2 Application of the maximum likelihood method

The basic idea is to maximize a likelihood function of the estimated probability distribution of the source ellipticities for a set of model parameters, given the functional form of the intrinsic ellipticity distribution measured for faint galaxies. We briefly outline the exact procedure below. From the simulated image frames we extract the observed ellipticity $\tau_{\rm obs}$. For each 'faint' galaxy j, the source ellipticity can then be estimated *in the weak regime* by just subtracting the lensing distortion induced by the smooth cluster and galaxy haloes given the parameters that characterize both these mass distributions: in other words,

$$\tau_{{\rm S}_j} = \tau_{{\rm obs}_j} - \Sigma_i^{N_c} \gamma_{{\rm p}_i} - \gamma_{\rm c}, \qquad (42)$$

where $\Sigma_i^{N_c} \gamma_{{\rm p}_i}$ is the sum of the shear contributions at a given position j from N_c perturbers, and the term γ_c is the shear induced by the smooth cluster component. In the strong regime, similarly, one can compute the source ellipticity using the inverse of equation (7). The lensing distortion depends on the parameters of the smooth cluster potential, on the perturbers and on the redshift of the observed arclet (lensed image), which is in general unknown. Therefore, in order to invert equation (7), for each lensed galaxy we need to assign a redshift, from a distribution of the form in equation (33) given the observed magnitude m_j, and take the mean of many such realizations. In principle, one needs also to correct the observed magnitude for amplification to obtain the true magnitude prior to drawing a redshift from $N(z, m)$, but this correction in turn depends on the redshift as well. An alternative procedure is then to correct for the amplification using the median z corresponding to the observed magnitude from the same distribution. This entire inversion procedure is performed within the lens tool utilities, which accurately takes into account the non-linearities arising in the strong regime. As an input for this calculation, we parametrize both the large-scale component and perturbing galaxies as described in Sections 2.2 and 3.1 respectively. Additionally, we assume that a well-determined 'strong lensing' model for the cluster-scale halo is known. For our analysis, we also assume that the functional form of $p(\tau_S)$ from the field is known, and is specified by equation (34); the likelihood for a guessed model can then be expressed as

$$\mathcal{L}(\sigma_{0*}, r_{t*}, ...) = \Pi_j^{N_{\rm gal}} p(\tau_{{\rm S}_j}). \qquad (43)$$

However, note that we ought to compute $\mathcal{L}$ for different realizations of the drawn redshift for individual images (say about 10–20) and then compute the mean of the different realizations of z_j; but it is easily shown to be equivalent to constructing the $\mathcal{L}$ for a single realization where the redshift z_j of the arclet drawn is the median redshift corresponding to the observed source magnitude. For the case when we perform a Monte Carlo sum over $N_{\rm MC}$ realizations of z_j, the likelihood is

$$\mathcal{L}(\sigma_{0*}, r_{t*}, ...) = \Pi_j^{N_{\rm gal}} \Pi_k^{N_{\rm MC}} p(\tau_{{\rm S}_j^k}), \qquad (44)$$

where $p_\tau(\tau_{{\rm S}_j^k})$ is the probability of the source ellipticity distribution at the position j for k drawings for the redshift of the arclet of known magnitude m_j. The mean value for $N_{\rm MC}$ realizations gives

$$\left\langle p(\tau_{{\rm S}_j}) \right\rangle = \frac{1}{N_{\rm MC}} \Sigma_{k=1}^{N_{\rm MC}} p\,(\tau_{{\rm S}_j^k}), \qquad (45)$$

which written out in integral form is equivalent to

$$\left\langle p(\tau_{{\rm S}_j}) \right\rangle = \frac{\int p\,[\tau_{{\rm S}_j}(z)] N(z, m_j)\,{\rm d}z}{\int N(z, m_j)\,{\rm d}z} = p[\tau_{{\rm S}_j}(z_{\rm avg})] \sim p[\tau_{{\rm S}_j}(z_{\rm median})], \qquad (46)$$

$z_{\rm avg}$ being the average redshift corresponding to the magnitude m_j. Therefore the corresponding likelihood $\mathcal{L}$ is then simply

$$\mathcal{L} = \Pi_j \left\langle p(\tau_{{\rm S}_j}) \right\rangle \qquad (47)$$

as before and the log-likelihood $l = \ln \mathcal{L} = \Sigma \left\langle p(\tau_{{\rm S}_j}) \right\rangle$. The best-fitting model parameters are then obtained by maximizing this log-likelihood function l with respect to the parameters σ_{0*} and r_{t*}, the characteristic central velocity dispersion and truncation radius

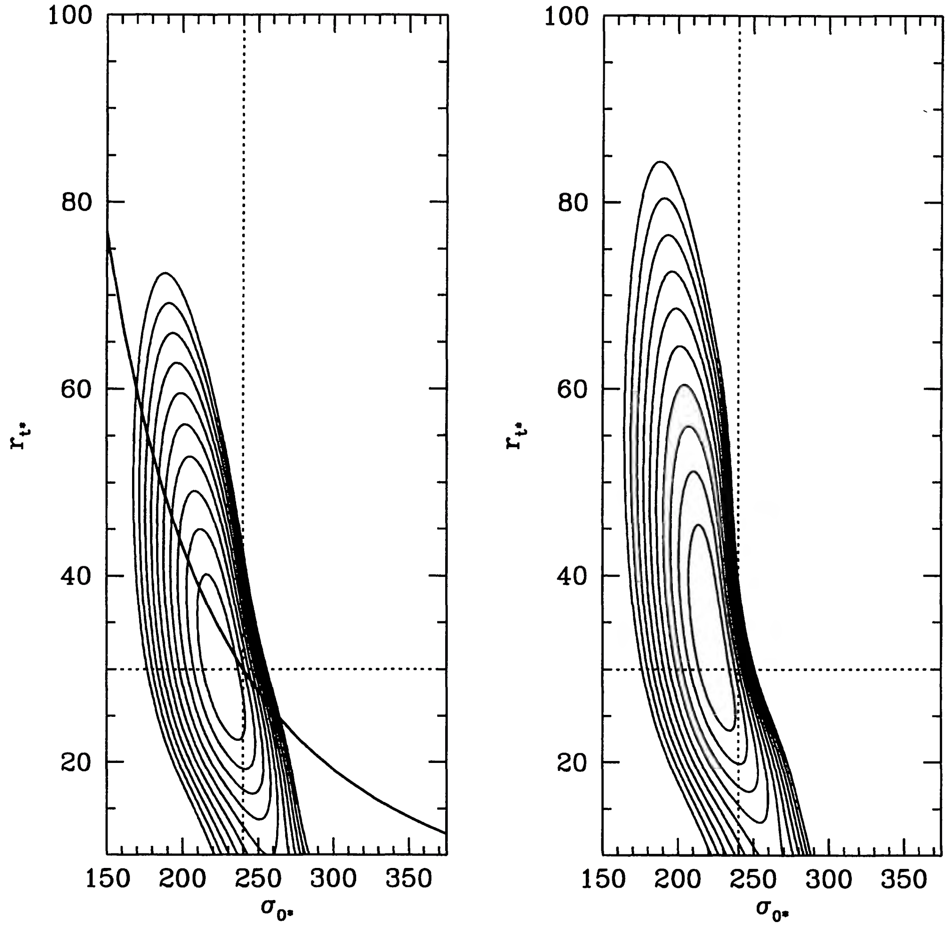

Figure 16. Log-likelihood contours for the retrieval of the fiducial parameters σ_{0*} and r_{t*} – the input values are indicated by the intersection of the dotted lines. Left panel: for the MDS ellipticity distribution, with assumed scaling $\alpha = 0.5$; right panel: the same with $\alpha = 0.8$.

respectively. The results of the maximization are presented in Figs 16–18. For all reasonable choices of input parameters we find that the log-likelihood function has a well-defined and broad maximum (interior to the innermost contour on the plots). The contour levels are calibrated such that $l_{max} - l = 1, 2, 3$ can be directly related to confidence levels of 63, 86, 95 per cent respectively (we plot only the first 10 contours for each of the cases in Figs 16–18) and the value marked by the dotted lines denotes the input values. In Fig. 16, we plot the likelihood contour for the MDS ellipticity distribution (equation 34). The left panel is for an assumed scaling law with $\alpha = 0.5$ and a constant mass-to-light ratio $\Upsilon = 12$. In the right panel, the corresponding contours for $\alpha = 0.8$ are plotted. For the MDS ellipticity distribution, we find that the velocity dispersion σ_{0*} can be more stringently constrained than the halo size, and the contours are elongated along the constant mass-to-light ratio curves and yield an output Υ very nearly equal to the input value. For narrower ellipticity distributions both the parameters can be constrained better and the inferred Υ is very nearly equal to the input value. We find that there is very little perceptible difference in the retrieval of parameters for the two cases with the different scaling laws. For a subcritical cluster (see bottom left panel in Fig. 18), we find that the parameters are recovered just as reliably, which is not surprising and in some sense illustrates the robustness of the maximum likelihood method. Thus, the physical quantity of interest that can be estimated best from the analysis above is the mass M_* of a fiducial L_* galaxy.

5.3 Estimating the required number of background galaxies

The largest source of noise in our analysis arises due to the finite number of objects in the frame. To estimate the required signal-to-noise ratio that would permit us to obtain reliable constraints on both σ_{0*} and r_{t*}, we reduced the number of background sources to 2500 keeping the number of lenses at 50 as before. We do not converge to a maximum in the log-likelihood, and consequently no confidence limits can be obtained on the parameters. Therefore, to apply this technique to the data we require the ratio r of the number of cluster galaxies to the number of background galaxies to be roughly $r < 0.2$, which can be achieved only by stacking the data from many clusters. Also, as found from the direct averaging procedure, we require ~5000 lensed images in order to detect securely $< \Upsilon > \geq 4$. Although typical *HST* cluster data fields of the order of 3×3 arcmin^2 have ~700 background galaxies (with a 10-orbit exposure), of these the shape parameters can be reliably measured only for about 200 galaxies, therefore on stacking the data from 20 (10-orbit) *HST* cluster fields, we should be able to constrain statistically the mean mass-to-light ratios as well as the two fiducial parameters.

5.4 Uncertainties in the smooth cluster component

In all of the above, we have assumed that the parameters that characterize the smooth cluster-scale component are very

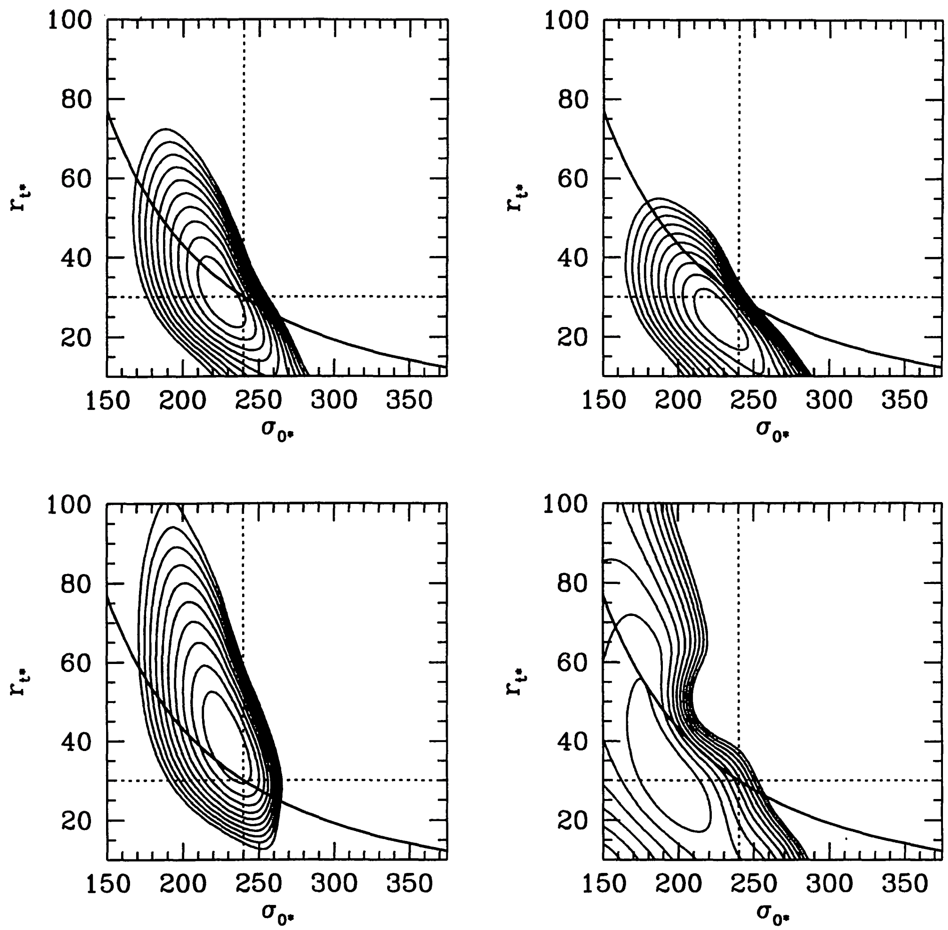

Figure 17. Sensitivity of log-likelihood contours to the strong lensing input parameters: examining the tolerance of the significance bounds obtained on σ_{0*} and r_{t*} with regard to the accuracy with which the cluster velocity dispersion needs to be known. All plots are for input $\Upsilon = 12$, $\alpha = 0.5$ and the MDS source ellipticity distribution. Top left panel: the exact value of the velocity dispersion is known (the value in this case is $1090\ \mathrm{km\,s^{-1}}$); top right panel: the velocity dispersion is known to within 2 per cent; bottom left panel: attempt to retrieve the incorrect scaling law – input $\alpha = 0.5$, log-likelihood maximized for $\alpha = 0.8$; bottom right panel: retrieval with fewer background galaxies.

accurately known, which is unlikely to be the case for the real data. We investigate the error incurred in retrieving the correct input parameters from not knowing this central strong lensing model well enough. So we can now place limits on the order of magnitude of errors that can be tolerated due to the lack of knowledge of the exact position of the cluster centre and the velocity dispersion of the main clump. In Fig. 18, we see that an uncertainty of the order of 20 arcsec in the position of the centre yields unacceptably incorrect values for σ_{0*} and r_{t*}. Conversely, if the centre is off by only 5 arcsec or so, for both the critical cluster and the subcritical one, the results remain unaffected and we obtain as good a retrieval of the input r_t^* as when the position of the centre is known exactly. Similarly, in Fig. 17, we demonstrate that an error of ~ 5 per cent in the velocity dispersion is enough to make the maximum likelihood analysis inconclusive, but an error of ~ 2–3 per cent at most would still enable us to obtain sensible bounds on both parameters.

6 CONCLUSIONS AND PROSPECTS

We conclude this paper and assert that both the maximum likelihood method and the direct averaging method developed in this paper can be feasibly applied to the real data on stacking a minimum of 20 WFPC2 deep cluster fields. These methods are well-suited to being used simultaneously as they are somewhat complementary; both yield the statistical mass-to-light ratio reliably and, while the averaging does not require the knowledge of either the centre or any details of the strong lensing model, it also cannot provide the decoupling of the two fiducial parameters, and hence no independent constraints on the velocity dispersion and the halo size can be obtained. Meanwhile the maximum likelihood approach permits estimation of the fiducial σ_{0*} and r_{t*} (σ_{0*} more reliably than r_{t*}), but it necessarily requires knowledge of the cluster centre and the central velocity dispersion rather accurately. In offset fields, however, where the gradient of the smooth cluster potential is constant over the smaller scales that we are probing, we expect both methods to perform rather well.

In this paper, we have not investigated the likely sources of error in the real data, which we will do in detail in a subsequent paper (Natarajan, Kneib & Smail, in preparation), but our simulations have enabled the study of the feasibility of application to *HST* cluster data regarding a statistical estimate of the number of background galaxies required for a significant detection, given the limitations in the accuracy to which the input parameters (like the strong lensing mass model and hence the magnification) are presently known. Our analysis points to the fact that the extraction of the signal would therefore be feasible if approximately 20–25 clusters were stacked, and the enterprise is especially suited to using the new ACS (Advanced Camera for Survey) due to be installed on

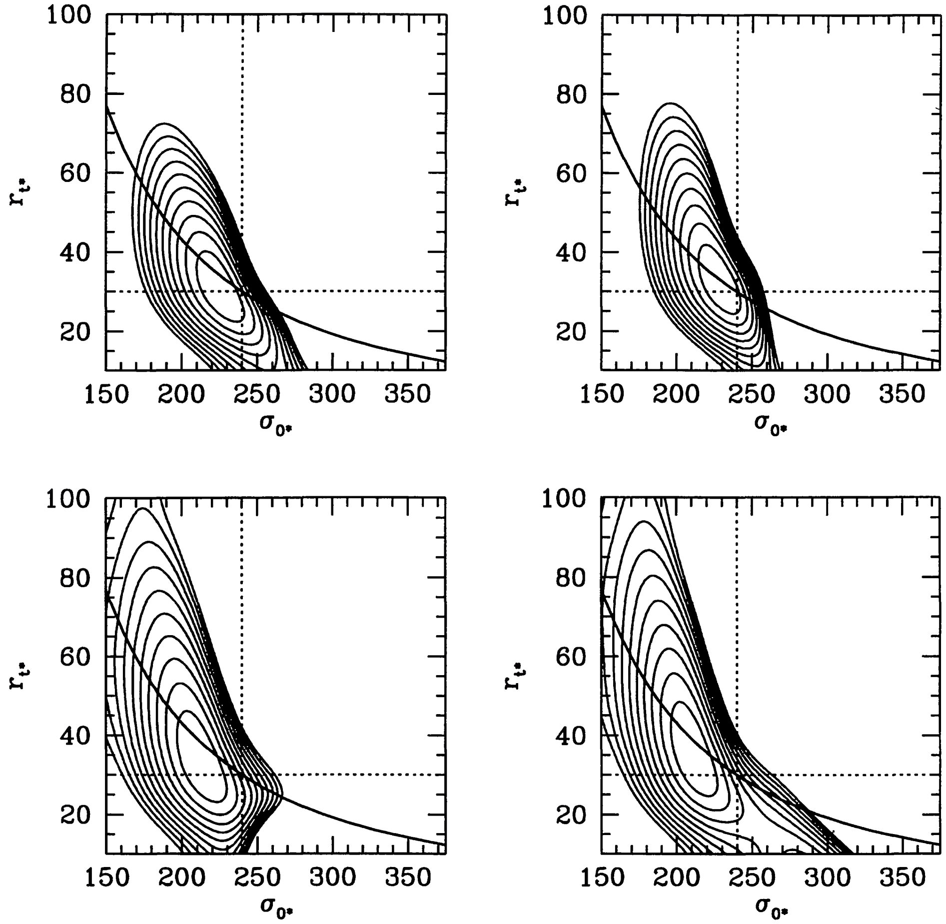

Figure 18. Sensitivity of the log-likelihood contours to input parameters: examining the tolerance of the significance bounds obtained on σ_{0*} and r_{t*} given the accuracy to which the cluster centre needs to be known. All plots are for input $\Upsilon = 12$, $\alpha = 0.5$ and the MDS source ellipticity distribution. Top left panel: knowing the cluster centre exactly for the critical cluster; top right panel: knowing the centre to within 5 arcsec; bottom left panel: knowing the centre exactly for the subcritical cluster; bottom right panel: for the subcritical cluster, centre known to within 5 arcsec.

HST in 1999. Additionally, since there exists a well-defined optimum lens redshift for signal detection ($0.1 < z_{\rm lens} < 0.3$), it might be useful to target clusters in this redshift range in future surveys in order to apply the techniques developed here. In our proposed analysis with the currently available *HST* data, we intend to incorporate parameters characterizing the smooth cluster (main clump) along with those of the perturbing galaxies into the maximum likelihood machinery.

In summary, we have presented a new approach to infer the possible existence of dark haloes around individual bright galaxies in clusters by extracting their local lensing signal. The composite lensing effect of a cluster is modelled in numerical simulations via a large-scale smooth mass component with additional galactic-scale masses as perturbers. The correct choice of coordinate frame, i.e. the local frame of each perturber, enables efficient subtraction of the shear induced by the larger scale component, yielding the averaged shear field induced by the smaller-scale mass component. Cluster galaxy haloes are modelled using simple scaling relations and the background high-redshift population is modelled in accordance with observations from redshift surveys. For several configurations of the sources and lens, the lensing equation is solved to obtain the resultant images. Not surprisingly, we find that the strength of the signal varies most strongly with the mass-to-light ratio of the cluster galaxies, and is only marginally sensitive to the assumed details of the precise fall-off of the mass profile. We also find that there is an optimum lens redshift range for detection of the signal. Although the entire procedure works in the 'strong lensing' regime as well, it is less noisy in the 'weak regime'. The proposed maximum likelihood method independently constrains the halo size and mass of a fiducial cluster galaxy, and we find that the velocity dispersion and hence the mass of a fiducial galaxy can be more reliably constrained than the characteristic halo size. Examining the feasibility of application to real data, we find that stacking $\sim$ 20 clusters allows a first attempt at extraction (Natarajan et al., in preparation). The prospects for the application of this technique are potentially promising, especially with sufficient and high-quality data (either *HST* images or ground-based observations under excellent seeing conditions of wider fields); the mass-to-light ratios of the different morphological/colour types in clusters, for instance, can be probed. More importantly, comparing with similar estimates in fields offset from the cluster centre would allow us to make the essential connections in order to understand the dynamical evolution of galaxies in clusters and the redistribution of dark matter within smaller scales within clusters. Application of this approach affords us the opportunity to probe the structure of cluster galaxies, as well as the efficiency of violent dynamical processes like tidal stripping, mergers and interactions which modify them and constitute the processes by which clusters assemble.

ACKNOWLEDGMENTS

PN thanks Martin Rees for his support and encouragement during the course of this work. We acknowledge useful discussions with Alfonso Aragon-Salamanca, Philip Armitage, Richard Ellis, Bernard Fort, Jens Hjorth, Yannick Mellier, Ian Smail and Simon White. PN acknowledges funding from the Isaac Newton Studentship and Trinity College; J-PK acknowledges support from an EC-HCM fellowship and from the CNRS.

REFERENCES

Abraham R. G., Tanvir N. R., Santiago B., Ellis R. S., Glazebrook K., van den Bergh S., 1996, MNRAS, 279, L47
Bird C., 1993, PASP, 105, 1495
Brainerd T., Blandford R., Smail I., 1996, ApJ, 466, 623
Broadhurst T., Taylor A. N., Peacock J., 1995, ApJ, 438, 49
Bruzual G., Charlot S., 1991, ApJ, 367, 126
Colless M., Dunn A., 1996, ApJ, 458, 435
Djorgovski G., Davis M., 1987, ApJ, 313, 59
Dressler A., Lynden-Bell D., Burstein D., Davies R. L., Faber S. M., Terlevich R. J., Wegner G., 1987, ApJ, 313, 42
Efstathiou G., Bernstein G., Tyson A., Katz N., Guhathakurta P., 1991, ApJ, 380, 47
Evrard A., Mohr J., Fabricant D., Geller M., 1993, ApJ, 410, L9
Fitchett M., 1988, in Dickey J., ed., The Minnesota lectures on clusters of galaxies and large-scale structure. Astron. Soc. Pac., San Francisco, p. 45
Glazebrook K., Ellis R. S., Santiago B., Griffiths R., 1994, BAAS, 185, 9505
Griffiths R., Casertano S., Ratnatunga K., Neuchafer L., 1994, ApJ, 435, L19
Griffiths R. E., Casertano S., Im M., Ratnatunga K. U., 1996, MNRAS, 282, 1159
Jorgensen I., Franx M., Kjaergaard P., 1996, MNRAS, 280, 167
Kaiser N., 1995, ApJ, 439 L1
Kaiser N., Squires G., 1993, ApJ, 404, 441
Kassiola A., Kovner I., 1993, ApJ, 417, 450
Kassiola A., Kovner I., Fort B., 1993, ApJ, 400, 41
Kneib J.-P., 1993, PhD thesis, Université de Toulouse III
Kneib J.-P., Ellis R., Smail I., Couch W., Sharples R., 1996, ApJ, 471, 643
Kriessler J., Beers T., Odewahn S., 1995, BAAS, 186, 07.02
Lilly S., Tresse L., Hammer F., Crampton D., Le Fevre O., 1995, ApJ, 455, L108
Natarajan P., Kneib J.-P., 1996, MNRAS, 283, 1031
Schneider P., 1995, A&A, 302, 639
Schneider P., Rix H., 1996, astro-ph/9601190, preprint
Schneider P., Seitz C., 1995, A&A, 294, 411
Smail I., Dressler A., Kneib J.-P., Ellis R., Couch W., Sharples R., Oemler A., 1995a, ApJ, 469, 508
Smail I., Hogg D., Yan L., Cohen J., 1995b, ApJ, 499, L105
Squires G., Kaiser N., 1996, ApJ, 473, 65
Tyson J. A., Valdes F., Jarvis J. F., Mills A. P., 1984, ApJ, 281, L59
West M., Bothun G., 1990, ApJ, 350, 36

This paper has been typeset from a TEX/LATEX file prepared by the author.